Addressing a Single Molecular Spin with Graphene-Based Nanoarchitectures

A. Candini, S. Lumetti, C. Godfrin, F. Balestro, W. Wernsdorfer, S. Klyatskaya, M. Ruben and M. Affronte

Abstract Finding reliable methods to exploit molecular degrees of freedom represents an intriguing problem involving the control of new mechanisms at the nanoscale and several technological challenges. Here, we report a novel approach to address a single molecular spin embedded in an electronic circuit. Our devices make use of molecules with well-defined magnetic anisotropy ($TbPc_2$) embedded in nanogapped electrodes obtained by electroburning graphene layers. Such devices work as molecular spin transistors allowing the detection of the Tb spin flip during the sweep of an external magnetic field. The spin readout is made by the molecular quantum dot that, in turns, is driven by an auxiliary gate voltage. In the general context of (spin-)electronics, these results demonstrate that: (1) molecular quantum dots can be used as ultra-sensitive detectors for spin flip detection and (2) the use of

A. Candini · S. Lumetti · M. Affronte (✉)
CNR, Istituto Nanoscienze, Centro S3, via G. Campi 213/A,
41125 Modena, Italy
e-mail: marco.affronte@unimore.it

S. Lumetti · M. Affronte
Dipartimento di Scienze Fisiche, Informatiche e Matematiche, Università degli Studi di Modena e Reggio Emilia, Via G. Campi 213A, 41125 Modena, Italy

C. Godfrin · F. Balestro · W. Wernsdorfer
Institut Néel, Université Grenoble Alpes, F-38042 Grenoble, France

C. Godfrin · F. Balestro · W. Wernsdorfer
CNRS, Institut Néel, F-38042 Grenoble, France

F. Balestro
Institut Universitaire de France, 103 Boulevard Saint-Michel,
75005 Paris, France

W. Wernsdorfer · S. Klyatskaya · M. Ruben
Institute of Nanotechnology, Karlsruhe Institute of Technology (KIT),
D-76344 Eggenstein-Leopoldshafen, Germany

M. Ruben
Institut de Physique et Chimie Des Matériaux de Strasbourg,
UMR 7504 UdS-CNRS, 67034 Strasbourg Cedex 2, France

T. Ogawa (ed.), *Molecular Architectonics*, Advances in Atom and Single Molecule Machines, DOI 10.1007/978-3-319-57096-9_8

graphene electrodes as a platform to contact organometallic molecules is a viable route to design more complex nanoarchitectures.

1 Introduction

The giant leaps in performance from the first computing machines to today's mobile devices are due to a large extent to the miniaturization of their active components. Currently, further downscaling is becoming an enormous technological challenge, since the device sizes are reaching the ultimate limit of the atomic and molecular scale. Experimental findings in electron transport through single molecules put forth the idea that the use of single molecules in electronics could represent the next goal of miniaturization of electronic devices [1]. Indeed, since the first proposal to use single molecules as an electronic component in 1974 [2], much effort has been put into downscaling devices to the single-molecule level. Three-terminal devices (transistors) constitute the reference elements for logic electronics, and in 2000, the first single-molecule transistor was realized [3]. In this molecular device, the current between source and drain passed through a single C_{60} molecule, and it was regulated by the voltage applied to the gate electrode.

On the single-molecule scale, the main advantage offered by the use of a gate electrode consists in the possibility to gain deeper insight into the electronic structure of the molecular system. By applying a voltage to the gate, it is indeed possible to change the electrostatic potential of the molecule, thereby shifting the energy of the molecular transport levels from which additional spectroscopic information about the molecule can be obtained, such as the presence of vibrational modes and excited states [3, 4]. Gate electrodes can also be used to change the charge state of a molecule (i.e., oxidize or reduce it) [5] and investigate higher-order transport processes such as co-tunneling and the Kondo effect [6, 7].

Despite the impressive progresses made in molecular electronics, addressing a single molecule still implies several technological challenges. The central one is certainly how to embed single molecules in electronic circuits in a reliable way suitable for mass production of devices [8]. Beside scanning probe techniques [9], the most popular approaches to fabricate molecular junctions are mechanical break junctions [10] and electromigrated junctions [11]. Gold is the preferred material for realizing such molecular electrodes, since it is a noble metal and it is (relatively) easy to handle. The use of gold, however, has several drawbacks: the high mobility of its atoms limits the stability of the junctions and their use for room temperature operations [8, 12, 13]. Moreover, the proximity of metal electrodes may significantly perturb the molecular energy levels [14]. Recently, the use of graphene as material for molecular-scale electrodes has been proposed as a valid alternative [1]. With respect to metallic contacts, graphene offers a planar geometry with a thickness comparable to the molecular size. Moreover, the possibility to exploit molecular functionalizations to attach the molecular units to the graphene electrodes via carbon bonds and/or π stacking looks straightforward from a chemical point of

view. Carbon-carbon bonds are expected to lower the energy gap between the chemical potential of the electrodes and the LUMO/HOMO molecular levels, thus decreasing the effective Schottky barrier at the molecular junction. Based on these considerations, several theoretical works have investigated the possibility to use graphene as an electrode to contact individual molecules [15–20], predicting specific features such as quantum coherent transport [15], edge effects [17], suppression of conductance fluctuations [18].

Recent pioneering works have demonstrated that it is possible to successfully use graphene for the realization of electrodes in molecular devices [21, 22]. More specifically, parallel multi-junctions devices have been fabricated in CVD graphene by using electron beam lithography and plasma etching [22–24]. In order to address individual molecules, the electroburning (EB) technique has been employed on exfoliated few-layer graphene on substrate, showing electrostatic molecular gating in molecular units at room temperature [21]. It is worth noting that the yield of fabrication of nm-sized gaps can be increased from about 50% [25] to more than 95% by performing the EB process under vacuum on single-layer graphene [26, 27].

Based on these premises, the choice of the graphitic architecture for molecular (spin-)electronics appears particularly appealing [1]. In view of scalable platforms suitable for a mass production of molecular-scale devices, the use of large area graphene actually appears as one of the most appropriate choices. However, most of the methods suitable for the production of large area graphene, such as chemical vapor deposition (CVD) [28], are optimized to obtain continuous films of monolayer graphene, whose electrical properties are strongly affected by the application of a gate bias. The use of few-layer graphene, which is still thin but much less gate dependent than single layer [21, 25], seems therefore preferable for molecular electronics.

While many electronic features have been studied so far by molecular devices, it is clear that specific magnetic features of molecules may actually act as an additional resource for logic circuits. In this context, single-molecule magnets constitute a particularly interesting class of molecules, as their magnetic properties provide a unique fingerprint to recognize the presence of a single molecule within a nanojunction [29–31]. Of particular interest here are molecules with well-defined magnetic anisotropy that can be easily recognized and exploited even at single-molecule level. A proposed prototypical device is therefore the molecular spin transistor [32], made of a single-electron transistor (SET) with non-magnetic electrodes and a single magnetic molecule as the conducting island.

Here, we report on the realization and functioning of three-terminal molecular devices in which a prototypical single-molecule magnet ($TbPc_2$) is embedded between two nanometer-spaced graphene-based electrodes. The bis(phthalocyanine) terbium(III) single-ion magnet ($TbPc_2$ hereafter, see Fig. 7a) has been already used for the realization of molecular spin transistors with gold electrodes, and it was shown how it is possible to read out the electronic and the nuclear spin of an isolated Tb^{3+} ion [30] as well as to coherently manipulate the nuclear spin [33]. For the electrodes, we chose to utilize graphene grown on the C-face of SiC [34–37] since it can be grown on large areas and displays a very small dependence on the

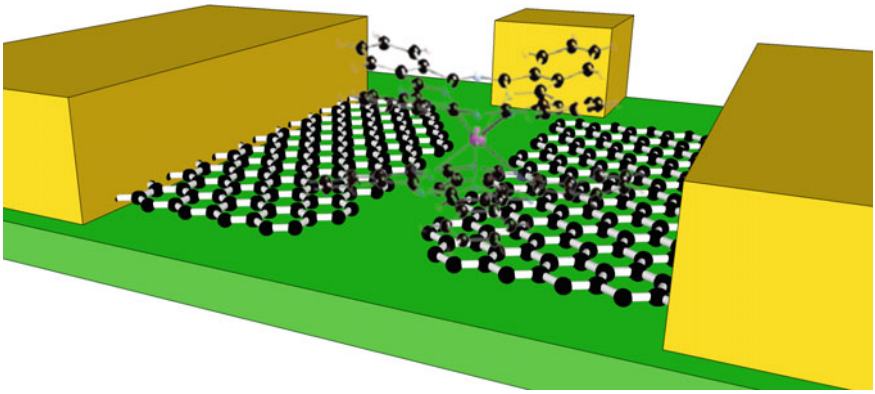

Fig. 1 Artistic view of the hybrid molecular device with graphene electrodes and a $TbPc_2$ magnetic molecule in the junction

external electric field. Molecular junctions are obtained by electroburning (see Sect. 3) with a gate electrode laterally approaching the nanogap (Fig. 1).

2 Molecular Spin Transistor

The functioning of a molecular spin transistor is schematized in Fig. 2. The energy spectrum of molecules is characterized by discrete electronic energy levels; therefore, the charge transport through such a device can be described as a quantum dot in the junction (Fig. 2). The presence of the electrodes (which act as reservoirs for charge carriers) causes the molecular states to hybridize with the states of graphene: electrons can therefore tunnel from and to the molecule with finite probability. When the energy broadening of the levels due to hybridization is smaller than the charging energy U of the molecule, then the molecule is weakly coupled to the electrodes. This is the case expected in using graphene electrodes. At low temperatures, electron transport is blocked (Fig. 3a) except for specific values of the gate voltage V_g bringing the molecular levels in resonance with the chemical potential of the electrodes (Fig. 3b) or for source–drain bias voltages aligning the chemical potential of one of the electrodes with a molecular level (Fig. 3c). This transport regime, known as Coulomb blockade, gives rise to large regions of suppressed conductance, forming characteristic Coulomb diamonds in differential conductance plots [38]. Vibrational and spin excitation states can lead to resonance levels and appear inside the diamonds as well, which makes transport measurements essentially a form of spectroscopy.

For the $TbPc_2$ molecule, a molecular quantum dot is formed in the organic Pc ligands. It is worth to note that in the neutral derivative $[TbPc_2]^0$ used in our experiments, there is an unpaired radical electron delocalized over the two Pc

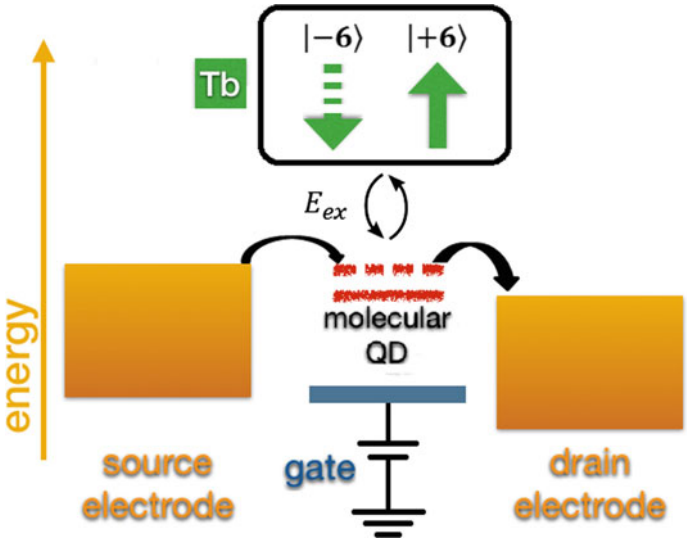

Fig. 2 Scheme of functioning for a molecular spin transistor. The molecule behaves as a quantum dot with a discrete spectrum of energy levels (*red lines*) which can be tuned by the gate potential (*blue*) and aligned to the Fermi level of the electrodes (*yellow*). The spin state of the metal center (Tb in the case of $TbPc_2$) affects the energy levels of the quantum dot by effectively changing the conductivity of the device for any spin flip event

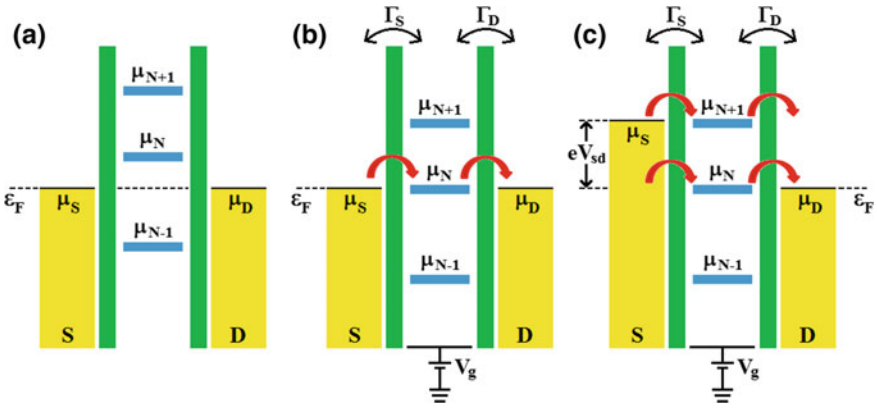

Fig. 3 Transport through a molecular junction (μ_N, μ_{N-1}, and μ_{N+1} denote the molecular levels, whereas μ_S and μ_D are the chemical potentials of source and drain electrodes, respectively). **a** Out of resonance, electrons cannot pass through the device. **b** Upon application of a gate voltage V_g, the molecular levels can be put in resonance with the chemical potentials of the electrodes and electrons can thus tunnel through the barrier. **c** By applying a bias voltage V_{sd}, the chemical potential of the electrodes is shifted and, as soon as it aligns with one or more molecular levels, the blockade is lifted and current flows (free elaboration from ref. [32])

ligands with spin S = 1/2 and this probably facilitates the creation of the molecular quantum dot, although other features may well induce charge transport through other molecules with no radical. It has been shown that the anisotropic magnetic moment of the Tb^{3+} ion is coupled to the organic Pc_2 ligands by an indirect exchange interaction [39]. Consequently, the energy levels of the molecular quantum dot, through which the charge is flowing, are split by the coupling with the Tb spin moment. At low temperatures, the Tb spin reversal is detected through jumps observed in the conductivity by sweeping the magnetic field.

Interestingly, these jumps are detected at very specific field values, corresponding to the allowed quantum tunneling resonances for the Tb electron spin, split by the hyperfine coupling with the nuclear moment (see Sect. 4). This mechanism allows for an unambiguous identification of the molecule under investigation.

3 Fabrication of Graphene-Based Electrodes

In the following, we describe the procedure we are using to realize the graphene-based electrodes. Turbostratic graphene is obtained on on-axis SiC (000-1) wafer according to a previously reported procedure [40, 41, 42]. Attenuation of the SiC signal in Raman spectra is used to estimate the number of grown layers [43], which are found to be about ten [44]. In addition, combined Raman and atomic force microscopy (AFM) analyses reveal a good homogeneity and quality of the resulting graphene [41, 44].

Electrical contacts are fabricated by electron beam lithography (EBL) through the following steps. Firstly, 3 nm Cr/30 nm Au are thermally deposited as the initial metal contacts in order to assure good ohmic contacts. Subsequently, graphene is patterned in the desired geometry by reactive ion etching (RIE) in an oxygen plasma. Finally, the connections from the initial metal contacts to the pads and the lateral gates are obtained by the evaporation of 5 nm Cr/50 nm Au.

Figure 4a, b show an overview of a typical pattern array, whereas the scanning electron microscope (SEM) image in Fig. 4c focuses on one of the graphene devices. The nanometer-sized gap in the graphene pads is finally opened via a feedback-controlled electroburning (EB) procedure [21] that can also be used for mechanically exfoliated flakes and chemically synthesized turbostratic graphene [44]. The EB process occurs thanks to the chemical reaction of carbon atoms with oxygen at high temperatures, induced by Joule heating at large current densities. The presence of a fast feedback loop (similar to what is employed for the electromigration of metallic nanowires [33, 45]) is vital to avoid the abrupt breaking of the junction, and it allows a precise control on the final structure of the molecular-sized junction.

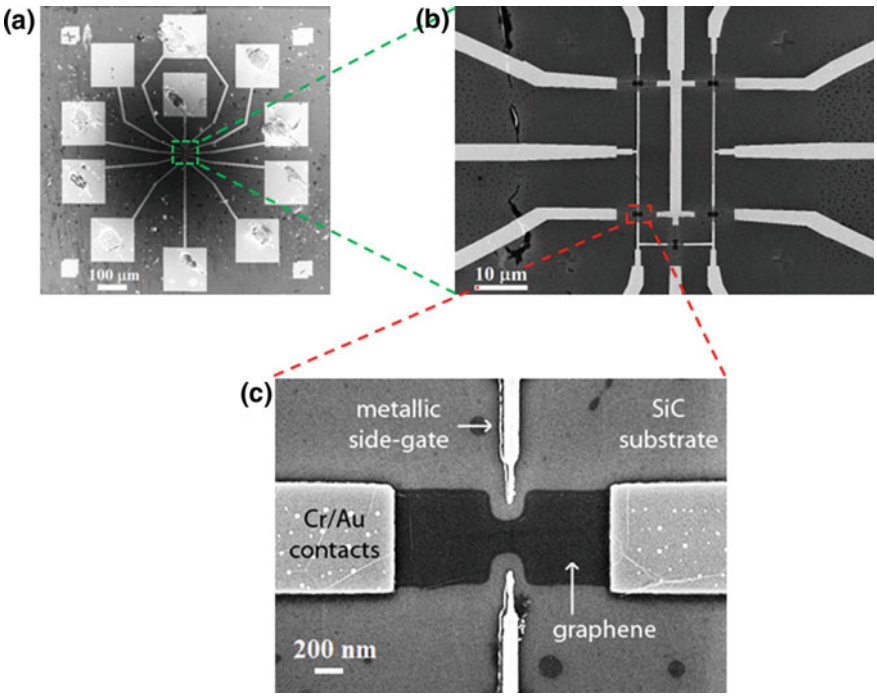

Fig. 4 **a**, **b** SEM images showing the typical lineup of metal pads and electrodes and related graphene-based architecture. **c** SEM image of a typical graphene device after fabrication: the middle "notched" graphene region is reduced to ~200 nm in width by plasma etching and the lateral gate electrodes are located at a distance of 50–100 nm

We perform the feedback-controlled EB in air at room temperature: an increasing voltage (V) ramp (typically 0.1 V/s) is applied to the graphene junction, while the current (I) is continuously recorded so that the variations in the resistance (R = V/I) can be monitored. As soon as R increases by more than a predefined percentage, the voltage is rapidly swept back to zero. Immediately after, a new sweep starts from zero voltage and the same process is repeated, thereby gradually narrowing the junction. The loop ends when the resistance measured at low bias is found to be above a certain predefined threshold.

Figure 5 shows a typical evolution of the feedback-controlled EB process. Normally, during the first voltage ramp (red trace in Fig. 5), nonlinear I-V characteristics are observed, probably due to the removal of contaminants by current annealing [26, 46]. The first EB event is induced by further increasing the voltage, as it can be inferred from the downward curvature in the I-V characteristics. When the resistance increase triggers the feedback control, the voltage is set back to 0 V and a new ramp is started. As the EB process evolves, the junction resistance

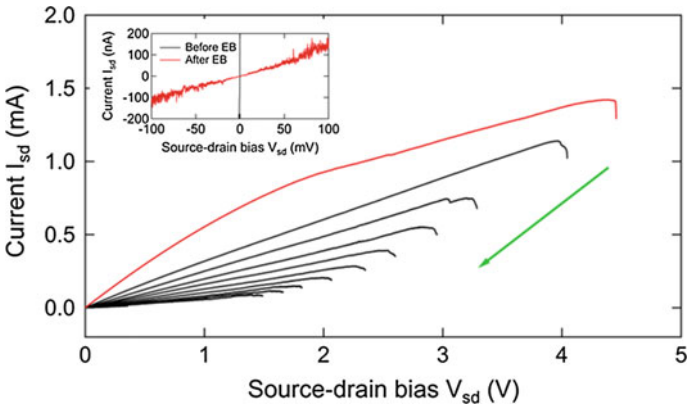

Fig. 5 Sequence of I-V characteristics during a feedback-controlled EB process. A voltage ramp is applied between source and drain contacts until a drop in the current is observed (EB onset), corresponding to a resistance increase by more than a predefined percentage within the last 100 mV. The feedback loop stops the process to avoid the complete burning of the junction and starts a new ramp immediately after. The resistance increases at each step until a threshold value is attained. The inset shows the current in the junction after the EB process

increases by steps and the voltage at which the EB occurs decreases (as indicated by the green arrow in Fig. 5).

With this EB process, it is possible to obtain graphene-based electrodes with nm-sized gaps displaying low-bias resistances in the range of 10^9–10^{10} Ω at room temperature. However, most of the experimental measurements on molecular devices are carried out at ultra-low temperatures (see Sect. 6). We have found that junctions with low-bias resistances higher than $\sim 10^6$ Ω at room temperature, typically, after the cooling, exhibit no tunneling current even up to high bias voltages of the order of 1 V, which is usually considered the signature of the creation of a large gap (>10 nm) not suitable for contacting one or few molecules. This effect is likely due to a mechanical contraction of the graphene electrodes when cooled down to cryogenic temperatures, which translates into an enlargement of the gap. To avoid this, we stop the EB process when the room temperature low-bias resistance is between $\sim 10^5$ and $\sim 10^6$ Ω. At this point, the I-V characteristics still have a finite linear slope (see inset of Fig. 5), suggesting that the gap formation is not yet complete. The final opening of the gap with size suitable to trap one or few molecules is achieved during the cooling.

In a first set of experiment, we have performed EB on 27 junctions of which 24 (89%) were controllably led to a low-bias resistance in the range of 100 kΩ to 3 MΩ. In the other cases, the feedback was not fast enough to respond, resulting in the formation of gaps with too high resistance (>1 GΩ).

Figure 6 shows a SEM image of a typical graphene junction after EB, cool down to ~100 mK and subsequent return to room temperature: a few nanometer-wide gap is visible in the central region of the graphene constriction. The fact that the gap

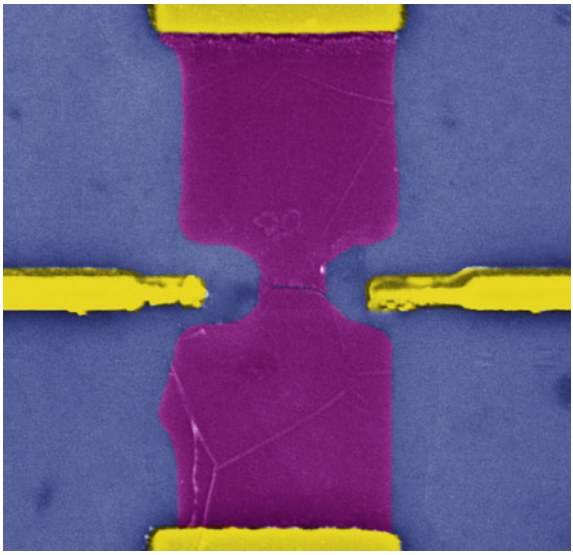

Fig. 6 Nanojunction in graphene electrode (false colors): a gap in the junction is visible at SEM after the EB process

opening occurs in the patterned middle region is not surprising: the reduced cross section ensures that, in that point, the current density has the largest value, which favors the rupture of graphene.

4 Molecule with Magnetic Fingerprint

$TbPc_2$ (Fig. 7a) is a prototypical case of single-ion magnetic molecule that has been largely used in several experiments thanks to its specific magnetic features and robustness when deposited on surfaces. Moreover, $TbPc_2$ perfectly suits to the single-molecule transistor configuration as adding one electron to the readout dot will not affect the charge state of the Tb ion, since this would require an oxidation or reduction of the terbium. Indeed, it was shown that up to the fifth reduction and second oxidation of the molecule, electrons are only added to the organic ligands [47]. The magnetic center of this molecule is a Tb^{3+} ion which has a ground state with a total magnetic moment $J = 6$ ($S = 3$, $L = 3$). In addition to the electronic spin, the Tb^{3+} ion carries a nuclear spin $I = 3/2$ with 100% abundance. The hyperfine interaction between the electron and the nuclear spin results in a fourfold splitting of each electronic level and introduces a dependence of the crossing point on the nuclear spin state.

The Hamiltonian describing the $TbPc_2$ molecular nanomagnet can therefore be written as the sum of three contributions: interaction with the ligand field, hyperfine coupling, and Zeeman effect (caused by the application of an external magnetic field).

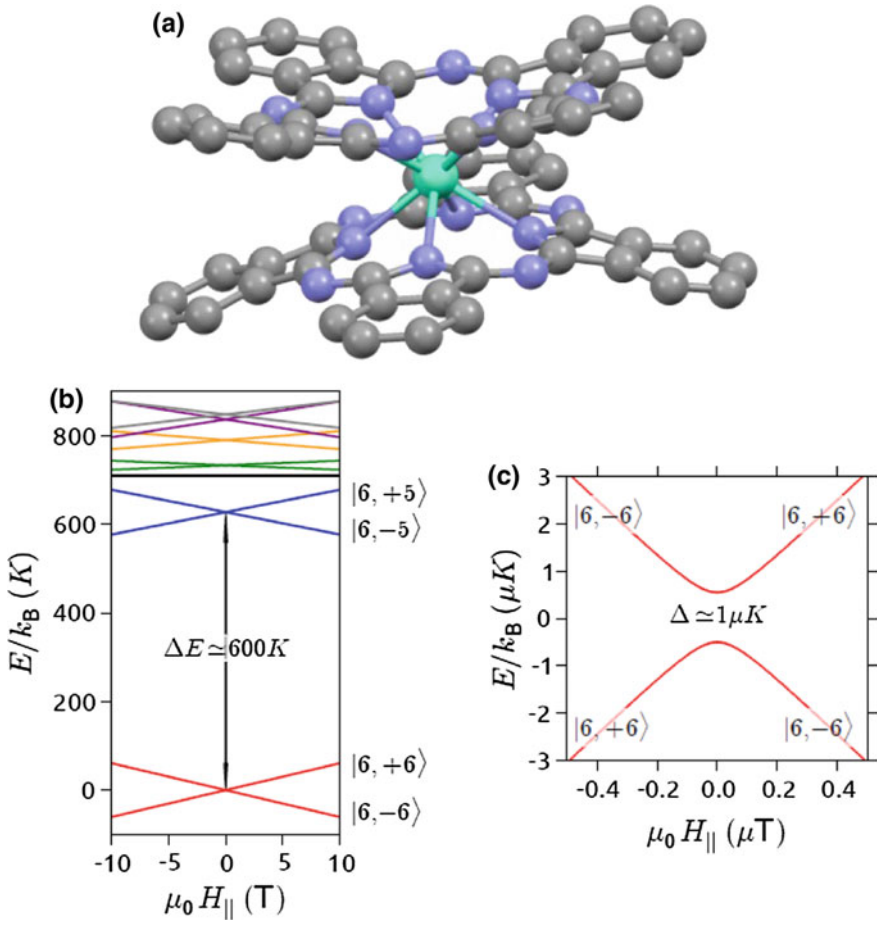

Fig. 7 **a** Molecular $TbPc_2$ double decker: Tb (*light green*), N (*light blue*); C (*gray*). **b** Zeeman diagram of the $TbPc_2$. The ligand field splits the ground state (*red*) and first excited state (*blue*) by about 600 K, leaving only two spin degrees of freedom at low temperature, which makes the $TbPc_2$ SMM an Ising-like quantum system. **c** Zoom on the ground state doublet. Off-diagonal terms in the ligand field Hamiltonian lift the degeneracy of the ground state doublet by $\Delta \sim 1$ μK and introduce an avoided level crossing in the Zeeman diagram

The magnetic moment of the Tb ion is subjected to a ligand field mainly defined by the length of its covalent bonds and by the symmetry of the SMM. Inside the complex, the Tb^{3+} ion is eightfold coordinated to the nitrogen atoms of the two

phthalocyanine ligands (see Fig. 7a). The Hamiltonian describing this ligand field interaction is given by [48]:

$$H_{LF} = A_2^0\langle r^2\rangle u_2 O_2^0 + \langle r^4\rangle u_4\left(A_4^0 O_4^0 + A_4^4 O_4^4\right) + A_6^0\langle r^6\rangle u_6 O_6^0$$

where the matrices O_k^q are the Stevens operators [49], $A_k^q\langle r^k\rangle$ the ligand field parameters [48, 50], and u_k the constant coefficients introduced by Stevens [51] and related to the ion ($u_2 = -1/99$, $u_4 = 2/16335$, $u_6 = -1/891891$). The terms O_k^0 contain the operator J_z up to the kth power and introduce a strong uniaxial anisotropy in the z direction.

When an external magnetic field $\boldsymbol{B}$ is applied to the single-molecule magnet, the effect on the energy levels can be described by the Zeeman Hamiltonian:

$$H_Z = g_J \mu_B J \cdot B$$

where $g_J = 1.5$ is the terbium's Landé g-factor and μ_B the Bohr magneton.

An exact numerical diagonalization of $H_{LF} + H_Z$ leads to the Zeeman diagram depicted in Fig. 7b [50]. The ligand field induces an energy gap of about 600 K between the ground state $|6, \pm 6\rangle$ and the first excited state $|6, \pm 5\rangle$. Hence, already at liquid nitrogen temperatures, the magnetic properties of this molecule are almost exclusively determined by the ground-state doublet $m_J = \pm 6$: the $TbPc_2$ SMM can thus be seen as an Ising-like spin system at low temperatures. The highly anisotropic character of the Tb spin can therefore be used as a fingerprint to recognize the actual presence of the molecule in the molecular transistor. Furthermore, the presence of the term $A_4^4\langle r^4\rangle u_4 O_4^4$ in H_{LF} is due to the fact that, because of π–π interactions between ligands, the two Pc planes are not exactly rotated by 45° [52]. This term does not modify the general behavior of the Zeeman diagram, but it mixes the $m_J = +6$ and $m_J = -6$ in third-order perturbation causing their degeneracy to be lifted by $\Delta \sim 1$ μK (see Fig. 7c). This avoided level crossing gives rise to zero field quantum tunneling of the magnetization.

Finally, the hyperfine interaction (coupling the electronic spin J with the nuclear spin I) and the nuclear anisotropy (accounting for the quadrupole moment of the nuclear spin due to the non-perfectly spherical shape of the nucleus) need to be included. The resulting hyperfine Hamiltonian H_{HF} is given by Ishikawa et al. [50]:

$$H_{HF} = AI \cdot J + P\left[I_z^2 - \frac{1}{3}I(I+1)\right]$$

where $I \cdot J = I_z J_z + \frac{1}{2}(I_+ J_- + I_- J_+)$, A is the hyperfine coupling strength and P the quadrupole moment of the nucleus. MicroSQUID measurements performed on $TbPc_2$ molecular crystals have shown that $A = 24.9$ mK and $P = 14.4$ mK [50].

The numerical diagonalization of the full Hamiltonian $H = H_{LF} + H_{HF} + H_Z$ at different magnetic fields results in the Zeeman diagram reported in Fig. 8a, where the eight lowest lying eigenstates are represented. Due to the hyperfine interaction,

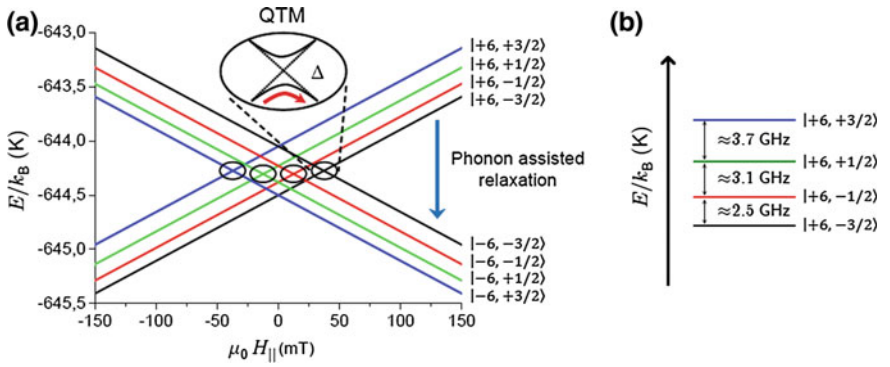

Fig. 8 **a** Zeeman diagram presenting the energy of the two ground states $J_z = \pm 6$ as a function of the magnetic field. Due to the hyperfine coupling with the nuclear spin $I = 3/2$, each electronic ground state is split into four. Lines with the same color correspond to the same nuclear spin state (*blue* $|+3/2\rangle$, *green* $|+1/2\rangle$, *red* $|-1/2\rangle$, *black* $|-3/2\rangle$). The *colored circles* indicate avoided level crossing between two states of opposite electronic spin and identical nuclear spin. **b** Energy spacing between the different nuclear spin states for electronic magnetic moment $J_z = +6$ at small magnetic fields

each electronic ground state is split into four. The lines with a positive (negative) slope correspond to the electronic spin $|+6\rangle(|-6\rangle)$ and lines with the same color to the same nuclear spin state. The splitting of the electronic levels is unequal due to the quadrupole term of the hyperfine interaction, as depicted in Fig. 8b. Moreover, the anticrossing, which was formerly at B = 0 T, is now split into four anticrossings, one for each nuclear spin state (see colored circles in Fig. 8a). The energy gap at each avoided level crossing remains about 1 μK.

Changing the external magnetic field parallel to the easy axis of the $TbPc_2$ allows for the reversal of the molecule's magnetic moment. There exist two completely different reversal mechanisms: a direct relaxation (which dominates at larger magnetic fields) and the quantum tunneling of magnetization (QTM, which is predominant at smaller magnetic fields).

QTM is a tunnel transition between two different spin states $|S, m_s\rangle$ and $|S, m_s'\rangle$. It requires a finite overlap of the two wavefunctions, which is caused by the off-diagonal terms in the Hamiltonian (in the case of $TbPc_2$, this is due to the ligand field that gives rise to an avoided level crossing). When sweeping the magnetic field over these anticrossings, the spin can tunnel from the $|S, m_s\rangle$ into the $|S, m_s'\rangle$ state with a probability P given by the Landau-Zener formula [53, 54].

In addition to the QTM, the magnetic moment of the molecule can reverse by a direct transition mechanism. This is an inelastic process involving the creation and/or the annihilation of phonons to account for energy and momentum conservation (this is why it is referred to as phonon-assisted or spin-lattice relaxation). Three types of relaxation processes can be distinguished depending on the temperature. At low T, the most likely spin reversal mechanism occurs through the emission of one phonon to the thermal bath (Fig. 9a). Increasing the temperature

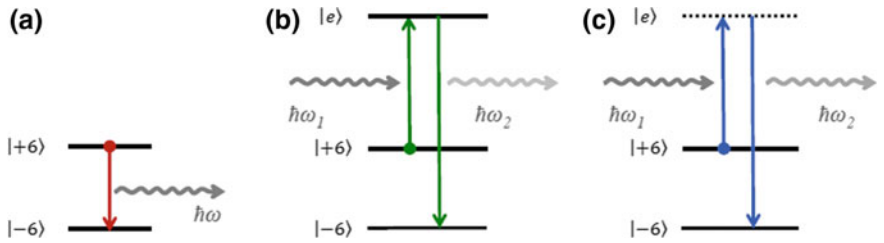

Fig. 9 Spin-lattice relaxation processes. **a** Direct relaxation into the ground state involving the emission of a phonon with energy $\hbar\omega$. **b** Two-phonon Orbach process, in which the molecule is excited into the state $|e\rangle$ via the absorption of a phonon of energy $\hbar\omega_1$ and subsequently emits another phonon of energy $\hbar\omega_2$, thereby relaxing into its ground state. **c** Two-phonon Raman process, similar to the Orbach one but involving a virtual excited state. Hyperfine splitting of the ground state doublet was omitted for simplicity

allows for a two-phonon relaxation process, in which the molecule is excited in a state $|e\rangle$ via the absorption of a phonon of energy $\hbar\omega_1$ and subsequently relaxes into the ground state through the emission of a phonon of energy $\hbar\omega_2$. This two-phonon relaxation mechanism is known as Orbach process (Fig. 9b) or Raman process (Fig. 9c) according to whether the excited state is real or virtual, respectively.

In order for a molecular magnet to be used in the framework of molecular spintronics, its magnetic properties need to be conserved when it is deposited on a conductive surface. XMCD (X-ray Magnetic Circular Dichroism) measurements performed on isolated $TbPc_2$ molecules on different surfaces confirmed the robustness of the magnetic properties of single molecules with respect to the adsorption on a conductive substrate [55, 39]. In realistic situations, $TbPc_2$ molecules between electrodes can be affected by torsional deformations [56], which slightly modify the term $A_4^4\langle r^4\rangle$ in the ligand field Hamiltonian thus possibly slightly modifying the energy gap at the avoided level crossings.

5 Realization of Molecular Devices

To obtain our devices, we start by fabricating nanogapped graphene electrodes, as described in detail in Sect. 3. $TbPc_2$ microcrystals are dissolved in dichloromethane, and the solution is sonicated in order for the remaining $TbPc_2$ clusters to be completely dissolved. Graphene junctions are cleaned using acetone and isopropanol, and then, some droplets of the solution are deposited on the SiC chip and blow-dried with nitrogen. Recent studies have shown that $TbPc_2$ molecules are adsorbed on surface with the phthalocyanine planes parallel to the surface plane [55]. Similar results have been reported for $TbPc_2$ on HOPG [57, 58]. However, due to the corrugation of the graphene surface and the presence of ripples (besides the local edge disorder introduced by electroburning), the orientation of the $TbPc_2$

molecule is expected to statistically present some misalignment leading to a finite tilt angle between the main device plane and the Pc plane [59].

6 Low-Temperature Experiments

Molecular spin transistors are cooled down to ~80 mK in a dilution fridge equipped with a 3D vector magnet allowing for magnetic field sweep rates up to 50 mT/s. Electrical measurements are carried out using the lock-in technique with an AdWin-Pro system (16-bit output and 18-bit input) and a FEMTO pre-amplifier.

Firstly, the low-temperature low-bias (1 mV) differential conductance dI/dV is measured as a function of the gate voltage V_g. The device typically exhibits an insulating behavior for all the accessible gate regions, except for one or few Coulomb peaks (two examples are provided in Fig. 10).

To characterize the charge transport through the device, both the bias and the gate voltage are swept, allowing for the construction of a differential conductance map. Figure 11 provides some examples. The stability diagrams exhibit typical Coulomb diamond-like characteristics, confirming that charge transport through our devices is in the Coulomb blockade regime and can be modeled by one or few quantum dots in parallel. Interestingly, the conductance map on the left of Fig. 11 is characterized by the presence of several excited states that are clearly visible as multiple lines running parallel to the Coulomb diamond's edges.

In a first set of experiments, after cooling, 5 out of 24 junctions (21%) exhibited Coulomb blockade-like features; 14 (58%) either showed no dependence on the applied gate voltage (albeit being characterized by a measurable tunneling current for $|V_{ds}| < 0.5$ V) or were in short circuit with one of the corresponding lateral gates. Finally, 5 devices (21%) displayed no tunneling current for $|V_{ds}| < 1$ V (open gaps between the two electrodes).

The spin properties of the $TbPc_2$ molecules are studied by the application of a magnetic field. Typically, only a small fraction of the tested devices (in our experiments < 10%) show a reliable magnetic signal. Focusing only on one specific sample, the differential conductance G(B) measured as a function of the magnetic

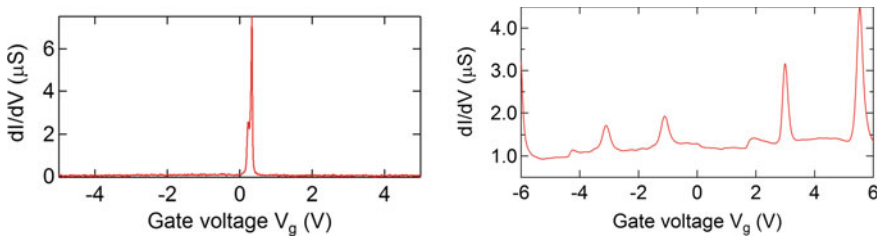

Fig. 10 Differential conductivity dI/dV as a function of the applied gate voltage for two different junctions. Some Coulomb peaks are visible

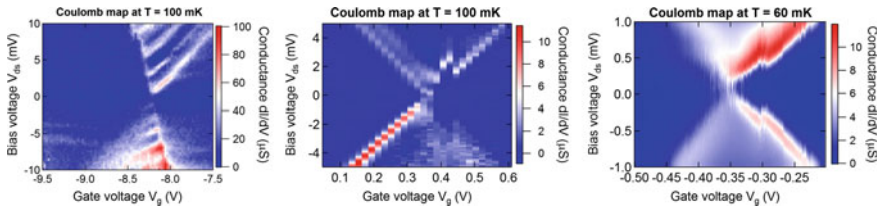

Fig. 11 Color scale plots of the differential conductance dI/dV as a function of gate voltage V_g and source–drain bias V_{ds} resulting from measurements performed on three different samples. The appearance of the characteristic Coulomb diamonds indicates that the transport is in the Coulomb blockade regime. In the map on the *left*, several excited states are visible as lines running parallel to the diamond edges

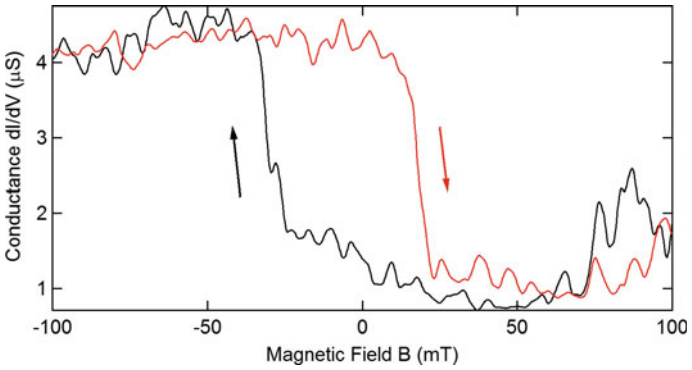

Fig. 12 Zero-bias differential magnetoconductivity of a $TbPc_2$ molecular spin transistor obtained at constant gate voltage (V_g is fixed at a value close to a charge degeneracy point). The black curve corresponds to the magnetoconductivity under increasing field (trace), while for the red one, the field is decreasing (retrace). The hysteresis is likely due to the magnetic moment reversal of the $TbPc_2$ SMMs deposited on the electroburnt graphene junctions

field shows the opening of a hysteresis loop (Fig. 12), showing clear jumps in the conductivity versus the external field.

The observed abrupt jumps in the conductance can be attributed to the switching of the $TbPc_2$ magnetic moment. As discussed in Sect. 2, the Pc ligands in the $TbPc_2$ molecule form a molecular quantum dot and the anisotropic magnetic moment of the Tb^{3+} ion is coupled to the electron path by an exchange interaction [39]. At low temperatures, the Tb spin reversal induces a shift in the energy levels of the Pc quantum dot that, in turns, provokes jumps in the conductivity by sweeping the magnetic field (see scheme Fig. 2). The mechanism of this electronic readout is therefore an indirect one: the current flows through one of the Pc ligands, which detects changes on the Tb electronic spin as a consequence of the exchange interaction.

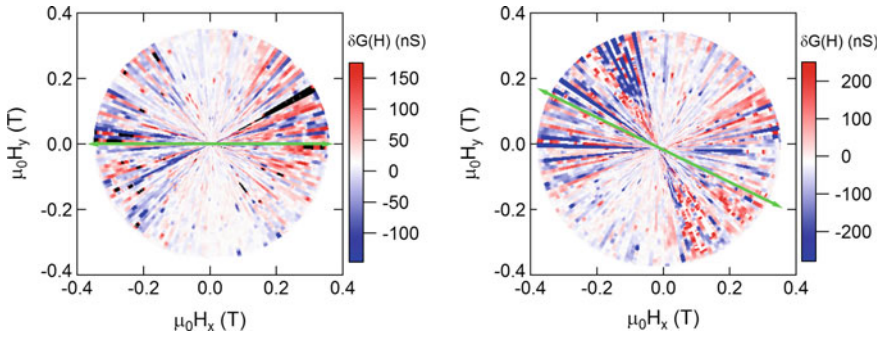

Fig. 13 Color plot of the difference δG(H) between trace and retrace for all directions of the magnetic field in the *xy* plane. The behavior is typical for magnetic systems exhibiting a uniaxial anisotropy. The easy axis is indicated by a *green arrow* and rotates by about 30° upon tilting the sample by 45°. Along the hard direction (perpendicular to the easy axis), no hysteresis is observed as the magnitude of the magnetic field is not high enough to reverse the magnetization of the system

The presence of the molecule between the graphene electrodes is confirmed by the study of the angular dependence of the magnetic jumps as a function of the magnetic field orientation. In Fig. 13, the difference δG(H) between the sweep up (trace) and down (retrace) of the magnetoconductance curves is plotted in color code for all the magnetic field directions in the (*xy*) plane of the device. The behavior reminds that of a magnetic system with uniaxial anisotropy and an easy axis of magnetization (indicated by a green arrow) can be identified. Upon a 45° tilt of the sample, the projection of the easy axis on the *xy* plane rotates by about 30°, suggesting that the field sweep direction is not exactly aligned with the easy axis itself.

As discussed in sect. 2, the origin of the magnetoconductance signal arises from the exchange coupling between the readout quantum dot and the electronic spin of the Tb^{3+} metal ion [33], leading to a splitting of the dot energy levels. Thus, the magnitude of the exchange coupling can be estimated by investigating the evolution of the splitting near a charge degeneracy point as a function of the applied magnetic field (Fig. 14). The splitting decreases linearly with increasing magnetic field and leads to a conductance peak at ~1.4 T which is the signature of the spin ½ Kondo effect due to an odd number of electrons in the readout quantum dot. The fact that the Kondo peak is split at zero magnetic field can be explained by a strong antiferromagnetic coupling to the terbium electronic spin. The magnitude of the coupling can be estimated via the formula [30]:

$$ag_J\mu_B J_z = k_B T_K + 2g\mu_B B_c$$

where g is the g-factor, μ_B the Bohr magneton, B_c the critical field (obtained extrapolating the Zeeman peaks at zero bias for positive values of the magnetic field), k_B the Boltzmann constant, T_K the Kondo temperature, $g_J\mu_B J_z$ the magnetic moment of the terbium, and a a positive constant accounting for antiferromagnetic

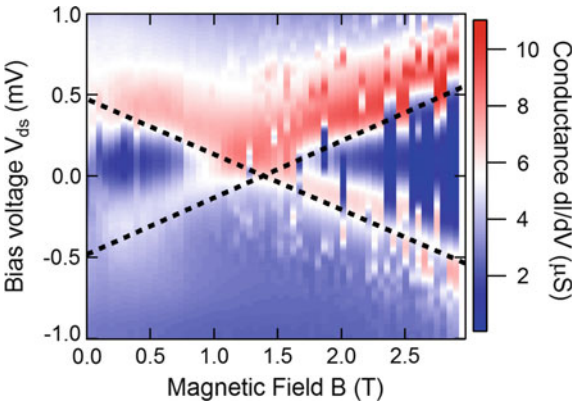

Fig. 14 Differential conductance measured as a function of the source–drain voltage and the magnetic field at fixed gate voltage. An exchange coupling constant $a \sim 1.1$ T can be extracted

coupling. The Kondo temperature can be estimated from the half width at half maximum (HWHM) of the Kondo signature at $B_c = 1.4$ T using the approximate expression $HWHM = k_B T_K / e$ [60]. Since HWHM $\sim$ 250 μV, a Kondo temperature $T_K \sim 2.9$ K can be inferred. By putting these values in the previous equation, a coupling constant $a \sim 1.10$ T can be derived. The efficient coupling between the two systems is probably due to the Pc unbound electron having S = ½ which is close in energy to the Tb 4f state [61].

7 Conclusions

The way things work at the molecular scale can be quite different from what we observe at the macroscopic scale due to the occurrence of both size and quantum effects. Thus, we need new concepts to design molecular devices. On top of this, we have to face extraordinary technological challenges to control matter and assemble devices at the single-molecule scale.

In this work, we have presented our recent results on the realization and test of novel molecular spin transistors. To have these devices working, we have adopted specific solutions that now need to be further tested. The key idea for having functioning devices is to use a molecular quantum dot as ultra-sensitive detector to reveal the spin reversal of a metal center tightly bound by exchange coupling. To validate our proposition, we have used a very special molecule, the so-called $[TbPc_2]^0$ single-ion magnet that, besides an extraordinary robustness, presents specific features such as the well-defined magnetic anisotropy of the Tb^{3+} ion and the presence of an unpaired electron delocalized over the two Pc ligands as a spin S = 1/2 radical. This scheme allows, in principle, to preserve the valence of the magnetic center while the charge current is passing through the molecular quantum dot. At the same time, exchange coupling guarantees a sufficiently strong coupling between the spin center and its detector. It will be interesting to test how these features are essential for the design of new generations of molecular spin transistors.

For the realization of the devices presented in this work, we have used junctions obtained in graphene electrodes by electroburning, instead of more conventional gold. Graphene presents a flat carbon surface which may favor the contact with organic molecules, and its chemical potential is expected to reduce the barrier at the molecular level, thus facilitating the electron conduction. Based on the results presented here, we believe that graphene can be considered as a suitable platform for contacting molecules and for the realization of complex electronic architectures at the molecular scale.

Acknowledgements This work has been partially supported by European Community through the FET-Proactive Project *"MoQuaS,"* contract N.610449; by the Italian Ministry for Research (MIUR) through the FIR grant RBFR13YKWX; and by the French Agency for Research through the ANR-12-JS10-007 SINUSManip, ANR-13-BS10-0001MolQuSpin projects and the Alexander von Humboldt foundation. We thank E. Bonet (Institut Néel, Grenoble, France) for help in software development, C. Coletti (IIT Pisa, Italy) for providing the graphene substrates and P. Pingue and F. Carillo (Scuola Normale Superiore di Pisa, Italy) for assistance in sample fabrication.

References

1. Sun, L., Diaz-Fernandez, Y.A., Gschneidtner, T.A., Westerlund, F., Lara-Avila, S. Moth-Poulsen, K.: Chem. Soc. Rev. **43**, 7378–7411 (2014). doi:10.1039/c4cs00143e
2. Aviram, A., Ratner, M.A.: Chem. Phys. Lett. **29**, 277 (1974). doi:10.1016/0009-2614(74)85031-1
3. Park, H., Park, J., Lim, A.K.L., Anderson, E.H., Alivisatos, A.P., McEuen, P.L.: Nature **407**, 57 (2000). doi:10.1038/35024031
4. Osorio, E.A., O'Neill, K., Stuhr-Hansen, N., Nielsen, O.F., Bjørnholm, T., van der Zant, H.S. J.: Adv. Mater. **19** (2), 281 (2007). doi:10.1002/adma.200601876
5. Kubatkin, S., Danilov, A., Hjort, M., Cornil, J., Bredas, N., Stuhr-Hansen, J.L., Hedegard, P., Bjørnholm, T.: Nature **425**, 698 (2003). doi:10.1038/nature02010
6. Park, J., Pasupathy, A.N., Goldsmith, J.I., Chang, C., Yaish, Y., Petta, J.R., Rinkoski, M., Sethna, J.P., Abruna, H.D., McEuen, P.L., Ralph, D.C.: Nature **417**, 722 (2002). doi:10.1038/nature00791
7. Liang, W.J., Shores, M.P., Bockrath, M., Long, J.R., Park, H.: Nature **417**, 725 (2002). doi:10.1038/nature00790
8. Lörtscher, E.: Nature Nanotechnol. **8**, 381–384 (2013). doi:10.1038/nnano.2013.105
9. Bumm, L.A., Arnold, J.J., Cygan, M.T., Dunbar, T.D., Burgin, T.P., Jones, T.P., Allara, D.L., Tour J.M., Weiss, P.S.: Science **271**, 1705–1707 (1996). doi:10.1126/science.271.5256.1705
10. Reed, M.A., Zhou, C., Muller, C.J., Burgin, T.P., Tour, J.M.: Science **278**, 252–254 (1997). doi:10.1126/science.278.5336.252
11. Park, H., Lim, A.K.L., Alivisatos, A.P., Park, J., McEuen, P.L.: Appl. Phys. Lett. **75**, 301–303 (1999). doi:10.1063/1.124354
12. Moth-Poulsen, K., Bjørnholm, T.: Nature Nanotechnol. **4**, 551–556 (2009). doi:10.1038/nnano.2009.176
13. Ratner, M.: Nat. Nanotechnol. **8**, 378–381 (2013). doi:10.1038/nnano.2013.110
14. Perrin, M.L., Verzijl, C.J.O., Martin, C.A., Shaikh, A.J., Eelkema, R., van Esch, J.H., van Ruitenbeek, J.M., Thijssen, J.M., van der Zant, H.S.J., Dulić, D., Nature Nanotechnol. **8**, 282–287 (2013)
15. Bergvall, A., Berland, K., Hyldgaard, P., Kubatkin, S., Löfwander, T.: Phys. Rev. B **84**, 155451 (2011). doi:10.1103/PhysRevB.84.155451

16. García-Suárez, V.M, Ferradás, R., Carrascal, D., Ferrer, J., Phys. Rev. B **87**, 235425 (2013). doi:10.1103/PhysRevB.87.235425
17. Ryndyk, D.A., Bundesmann, J., Liu, M.-H., Richter, K.: Phys. Rev. B **86**, 195425 (2012), doi:10.1103/PhysRevB.86.195425
18. Péterfalvi, C. G., Lambert, C. J.: Phys. Rev. B **86**, 085443 (2012), doi:10.1103/PhysRevB.86.085443
19. Prasongkit, J., Grigoriev, A., Pathak, B., Ahuja, R., Scheicher, R.H.: J. Phys. Chem. C **117**, 15421–15428 (2013). doi:10.1021/jp4048743
20. Pshenichnyuk, I.A., Coto, P. B., Leitherer, S., Thoss, M.: J. Phys. Chem. Lett. **4**, 809–814 (2013). doi:10.1021/jz400025q
21. Prins, F., Barreiro, A., Ruitenberg, J.W., Seldenthuis, J.S., Aliaga-Alcalde, N., Vandersypen, L.M.K., van der Zant, H.S.J.: Nano Lett. **11**, 4607–4611 (2011). doi:10.1021/nl202065x
22. Cao, Y., Dong, S., Liu, S., He, L., Gan, L., Yu, X., Steigerwald, M. L., Wu, X., Liu, Z., Guo, X.: Angew. Chem. Int. Ed. **51**, 12228–12232 (2012). doi:10.1002/anie.201205607
23. Jia, C., Wang, J., Yao, C., Cao, Y., Zhong, Y., Liu, Z., Liu, Z., Guo, X.: Angew. Chem. Int. Ed. **52**, 1–6 (2013). doi:10.1002/anie.201304301
24. Cao, Y., Dong, S., Liu, S., Liu, Z., Guo, X.: Angew. Chem. Int. Ed. **52**, 3906–3910 (2013). doi:10.1002/anie.201208210
25. Burzurí, E., Prins, F., van der Zant, H.S.J., Graphene **01**, 26–29 (2012). doi:10.4236/graphene.2012.12004
26. Nef, C., Pósa, L., Makk, P., Fu, W., Halbritter, A., Schönenberger, C., Michel, C.: Nanoscale **6**, 7249–7254 (2014). doi:10.1039/c4nr01838a
27. Lau, C.S., Mol, J.A., Warner, J.H., Briggs, G.A.D.: Phys. Chem. Chem. Phys. **16**, 20398–20401 (2014). doi:10.1039/c4cp03257h
28. Kim, K.S., Zhao, Y., Jang, H., Lee, S.Y., Kim, J.M., Kim, K.S., Ahn, J.-H., Kim, P., Choi, J.-Y., Hee, B.: Nature **457**, 706 (2009). doi:10.1038/nature07719
29. Zyasin, A.S., van den Berg, J.W.G., Osorio, E.A., van der Zant, H.S.J., Konstantinidis, N.P., Leijnse, M., Wegewijs, M.R., May, F., Hofstetter, W., Danieli C., Cornia A.: Nano Lett. **10**, 3307 (2010). doi:10.1021/nl1009603
30. Vincent, R., Klyatskaya, S., Ruben, M., Wernsdorfer, W., Balestro, F.: Nature **488**, 357 (2012). doi:10.1038/nature11341
31. Burzurí, E., Zyasin, A.S., Cornia, A., van der Zant, H.S.J.: Phys. Rev. Lett. **109**, 147203 (2012). doi:10.1103/PhysRevLett.109.147203
32. Bogani, L., Wernsdorfer, W.: Nat. Mater. **7**, 179–186 (2008). doi:10.1038/nmat2133
33. Thiele, S., Balestro, F., Ballou, R., Klyatskaya, S., Ruben, M., Wernsdorfer W.: Science **344**, 1135–1138 (2014). doi:10.1126/science.1249802
34. Forbeaux, I., Themlin, J.M., Debever, J.M.: Phys. Rev. B **58**, 16396–16406 (1998). doi:10.1103/PhysRevB.58.16396
35. Berger, C., Song, Z., Li, T., Li, X., Ogbazghi, A.Y., Feng, R., Dai, Z., Marchenkov, A.N., Conrad, E.H., First, P.N., de Heer, W.A.: J. Phys. Chem. B **108**, 19912–19916 (2004). doi:10.1021/jp040650f
36. Ohta, T., Bostwick, A., Seyller, T., Horn, K., Rotenberg, E.: Science **313**, 951–954 (2006). doi:10.1126/science.1130681
37. Virojanadara, C., Syväjarvi, M., Yakimova, R., Johansson, L.I., Zakharov, A.A., Balasubramanian, T.: Phys. Rev. B, **78**, 245403 (2008). doi:10.1103/PhysRevB.78.245403
38. Hanson, R., Kouwenhoven, L.P., Petta, J.R., Tarucha, S., Vandersypen, L.M.K.: Rev. Mod. Phys. **79**, 1217–1265 (2007). doi:10.1103/RevModPhys.79.1217
39. Candini, A., Klar, D., Marocchi, S., Corradini, V., Biagi, R., De Renzi, V., del Pennino, U., Troiani, F., Bellini, V., Klyatskaya, S., Ruben, M., Kummer, K., Brookes, N.B., Huang, H., Soncini, A., Wende, H., Affronte, M.: Sci. Rep. **6**, 21740 (2016)
40. Frewin, C.L., Coletti C., Riedl, C., Strake, U., Saddow, S.E.: Mater. Sci. Forum **615–617**, 589-592 (2009). doi:10.4028/www.scientific.net/MSF.615-617.589
41. Starke, U., Forti, S., Emtsev, K.V., Coletti, C.: MRS Bull. **37**, 1177–1186 (2012). doi:10.1557/mrs.2012.272

42. Convertino, D., A. Rossi., V. Miseikis, V., Piazza, C., Coletti., Thermal decomposition and chemical vapor deposition: a comparative study of multi-layer growth of graphene on SiC (000-1). MRS Advances **1** (55), 3667–3672 (2016)
43. Shivaraman, S., Chandrashekhar, M.V.S., Boeckl, J.J., Spencer, M.G.J.: Electron. Mater. **38**, 725–730 (2009). doi:10.1007/s11664-009-0803-6
44. Candini, A., Richter, N., Convertino, D., Coletti, C., Balestro, F., Wernsdorfer, W., Kläui, M., Affronte, M.: Beilstein J. Nanotechnol. **6**, 711–719 (2015). doi:10.3762/bjnano.6.72
45. Prins, F., Hayashi, T., van Steenwijk, B.J.A.D., Gao, B., Osorio, E.A., Muraki, K., van der Zant, H.S.J.: Appl. Phys. Lett. **94**, 123108 (2009). doi:10.1063/1.3109784
46. Moser, J., Barreiro, A., Bachtold A.: Appl. Phys. Lett. **91**, 163513 (2007). doi:10.1063/1.2789673
47. Zhu, P., Lu, F., Pan, N., Arnold, D. P., Zhang, S., Jiang, J., Eur. J. Inorg. Chem. **2004**, 510–517 (2004). doi:10.1002/ejic.200300509
48. Ishikawa, N., Sugita, M., Okubo, T., Tanaka, N., Iino, T., Kaizu, Y., Inorg. Chem. **42**, 2440–2446 (2003). doi:10.1021/ic026295u
49. Abragam, A., Bleaney, B.: Electron Paramagnetic Resonance of Transition Ions (Oxford Classic Texts in the Physical Sciences). Oxford University Press, New York (2012). ISBN 978-0-19-965152-8
50. Ishikawa, N., Sugita, M., Wernsdorfer, W.: Angew. Chem. Int. Ed. **44**(19), 2931–2935 (2005). doi:10.1002/anie.200462638
51. Stevens, K. W. H.: Proc. Phys. Soc. A **65**, 209–215 (1952). doi:10.1088/0370-1298/65/3/308
52. Koike, N., Uekusa, H., Ohashi, Y., Harnoode, C., Kitamura, F., Ohsaka, T., Tokuda, K.: Inorg. Chem. **35**(20), 5798–5804 (1996). doi:10.1021/ic960158d
53. Landau, L.D.: Phys. Sov. Union **2**, 46–51 (1932)
54. Zener, C.: *Proc. R. Soc. Lond. A* **137**, 696–702 (1932). doi:10.1098/rspa.1932.0165
55. Stepanow, S., Honolka, J., Gambardella, P., Vitali, L., Abdurakhmanova, N., Tseng, T.-C., Rauschenbach, S., Tait, S.L., Sessi, V., Klyatskaya, S., Ruben, M., Kern, K.: J. Am. Chem. Soc. **132**(34), 11900–11901 (2010). doi:10.1021/ja105124r
56. Sorace, L., Benelli, C., Gatteschi, D.: Chem. Soc. Rev. **40**, 3092–3104 (2011). doi:10.1039/C0CS00185F
57. Gopakumar, T.G., Muller, F., Hietschold, M.: J. Phys. Chem. B **110**, 6051–6065 (2006). doi:10.1021/jp060936f
58. Klar, D., Candini, A., Joly, L., Klyastkaya, S., Krumme, B., Ohresser, P., Kappler, J.-P., Ruben, M., Wende, H.: Dalton Trans. **43**, 10686–10689 (2014)
59. Candini, A., Klyatskaya, S., Ruben, M., Wernsdorfer, W., Affronte, M.: Nano Lett. **11**, 2634–2639 (2011). doi:10.1021/nl2006142
60. Scott, D.G., Natelson, D.: ACS Nano **4**(7), 3560–3579 (2010). doi:10.1021/nn100793s
61. Vitali, L., Fabris, S., Conte, A.M., Brink, S., Ruben, M., Baroni, S., Kern, K., Nano Lett. **8**, 3364–3368 (2008). doi:10.1021/nl801869b